Multiple transition metals modulated hierarchical networks for high performance of metal-ion batteries

Jie Liu [a], Chenjie Lou [a], Jipeng Fu [a,b], Xuan Sun [b], Jingrong Hou [c], Jiwei Ma [c], Yongjin Chen [a], Xiang Gao [a], Ligang Xu [d], Qi Wei [d], Mingxue Tang [a,*]

HPSTAR
1422-2022

[a] *Center for High Pressure Science and Technology Advanced Research, Beijing 100094, China*
[b] *Institute of Optoelectronic Materials and Devices, China Jiliang University, Hangzhou 310018, Zhejiang, China*
[c] *Institute of New Energy for Vehicles, School of Materials Science and Engineering, Tongji University, Shanghai 201804, China*
[d] *College of Materials Science and Engineering, Beijing University of Technology, Beijing 100124, China*

ARTICLE INFO

ABSTRACT

Searching anodes with excellent electrochemical performance has been in great demand for rechargeable metal ion batteries. In this contribution, Fe/Co co-doped NiS with N-based carbon (FeCo-NiS@NC) derived from trimetallic Prussian blue analogue is designed and synthesized. The composition can be easily adjusted and modulated by multi-metals. In addition, the well-designed carbon nanocubes effectively promote electronic conductivity and buffer the volume change upon charge and discharge cycling, resulting in good capacity and long-term cycle life for both lithium-ion batteries and sodium-ion batteries, with capacities of 1018 mAh g^{-1} (vs. Li/Li$^+$) and 454 mAh g^{-1} (vs. Na/Na$^+$), respectively, after 100 cycles. Kinetics studies indicate that the electrochemical behaviors are manipulated by both diffusion and pseudocapacitance processes. These strategies would open new opportunities and potention for novel energy storage.

© 2022 Science Press and Dalian Institute of Chemical Physics, Chinese Academy of Sciences. Published by ELSEVIER B.V. and Science Press. All rights reserved.

1. Introduction

Lithium-ion batteries (LIBs) have been explosively utilized in many portable energy devices due to their remarkable advantages in terms of high energy density, long cycle life, environment-friendly, and small radius for fast cycling [1–3]. In the meanwhile, sodium-ion batteries (SIBs), with lower cost and abundant source, were also considered as potential alternative energy storage due to their similar features as LIBs [4,5]. Although much effort has been dedicated to searching materials with excellent electrochemical performance, there is still a wide gap existing to obtain anodes with high specific capacity, suitable operating potential, and outstanding cycling stability [6].

Intercalation, alloying and conversion processes are mainly reaction mechanisms that occur to anodes [7]. The materials with intercalation mechanism are hard to serve as anodes for both lithium and sodium ion batteries simultaneously because of different radii for Li and Na atoms to accommodate [8]. For example, the specific capacity of commercial graphite for LIBs is 372 mAh g^{-1},

but only 35 mAh g^{-1} can be obtained for SIBs. The second type of anode materials with alloying reaction encounters huge volume variation during electrochemical cycling, further resulting in structural instability and capacity decay [5]. When turning to the anode materials with conversion mechanism, such as metal oxide [9–14], metal sulphides [15–22], metal phosphides [23–28], and metal selenide [21,22], they satisfy the requirements of both high energy density and high power density. Particularly, transition metal sulphides (MSs) such as MoS$_2$ [17,29,30], CoS$_2$[31], FeS$_2$ [19,32], MnS [33], CuS [34,35], NiS$_x$ [36,37] etc., have been considered as promising anode materials for LIBs and SIBs attributed to the properties of easy preparation, high capacity and decent electrochemical reversibility [38]. In addition, MSs are more suitable to store metal ions with larger radius, such as Na$^+$ [33]. Although the working potential plateau of metal sulfides is relatively too high for ideal anodes, many academic efforts have been devoted to further improving the electrochemical activities in terms of stability, rate performance, and energy density. However, many issues of such materials are still unsolved: (1) the transition metal sulphides suffer low electronic conductivity and ion migration kinetics [20], and (2) the majority of metal sulphides show intensive capacity decay because of severe volume change during the charge/discharge process [39]. Many approaches have been tried to address the above

---

* Corresponding author.
  E-mail address: mingxue.tang@hpstar.ac.cn (M. Tang).

problems: (1) coating carbon shell or choosing appropriate carbon base to improve electronic conductivity for enhancing rate performance, and (2) constructing nanostructure to efficiently buffer structure/volume change for maintaining reversible capacity. Xu et al. designed FeS_2 nanocrystal, which is protected by nitrogen doped carbon and encapsulated into three-dimensional graphene, and the composite material delivers ultrahigh reversible capacities for both LIBs and NIBs [19]. However, the graphene oxide is too expensive to use in practical application. Moreover, doping and substituting metal elements can modulate hierarchical nanostructure and greatly improve electrochemical properties by synergetic effects from multi-metallic elements. Lou et al. constructed an integrated nanostructure through metal-organic frame (MOF) templating strategy to form Cu-substituted $CoS_2@Cu_xS$, which shows decent electrochemical properties for SIBs [35]. But the preparation process of such kind of material is slightly complicated. As such, it is a great advance by combining all the merits together to design novel anodes with satisfied properties for metal-ion batteries. However, there are rare reports on three and/or more transition metals coexist for satisfied anodes. In this study, we carefully designed MSs that cofined in carbon nanocubes, enhancing fast electron conductivity and leaving inside voids for buffering the volume change during electrochemical cycling. Multiple transition metals (Fe, Co, and Ni) are introduced into the core MSs for enhanced rate performance and capacity.

Herein, Fe and Co co-doped NiS with N-based carbon (FeCo-NiS@NC) derived from trimetallic Prussian blue analogue (FeCoNi-PBA) was designed and synthesized. The obtained FeCo-NiS@NC anode material exhibits predominant electrochemical performance during de/lithiation and de/sodiation processes for LIBs and SIBs, respectively. X-ray diffraction (XRD) and nuclear magnetic resonance (NMR) were carried out to probe the cycling reaction mechanisms and morphology studies address the cycling stability and boost capacity.

2. Experimental

2.1. Materials

(1) Synthesis of trimetallic Prussian blue analogues (PBA). According to our previous study [40], 3 mmol nickel nitrate hexahydrate and 4.5 mmol sodium citrate were dissolved in 100 mL deionized water (denoted as solution A). 1 mmol potassium ferricyanide and 1 mmol potassium hexacyanocobaltate were added in 100 mL deionized water to form solution B. Solution B was further added into solution A with magnetic stirring for about 5 min. The mixed solution was aged overnight and was separated by centrifugation. The product was washed with deionized water and ethyl alcohol three times, followed by drying at 70 °C under vacuum overnight.

(2) Synthesis of PBA@PDA composite. 200 mg of the synthesized PBA was dissolved in 200 mL tris buffer solution (PH = 8.5) under magnetic stirring for ∼5 min. Then 200 mg dopamine hydrochloride was added directly with stirring for 12 h. The final black production, polydopamine (PDA) coated Prussian blue analogue (PBA@PDA), was collected by centrifugation and dried in vacuum oven at 70 °C overnight.

(3) Synthesis of FeCo-NiS@NC and FeCo-NiS. The target products were obtained by treating the previously obtained PBA@PDA at high temperature. The PBA@PDA was firstly presintered at 350 °C for 2 h under Argon atmosphere. 100 mg pure sulphur was encapsulated in small box made by Ti mesh, surrounding by 50 mg presindered samples in porcelain boat. The boat was subsequently sintered at 600 °C for 2 h with a heating rate of 5 °C min^{-1} under Argon atmosphere. The final product is FeCo-doped NiS

coated with N-doped carbon shell (FeCo-NiS@NC). The FeCo-NiS was prepared in a similar way of making FeCo-NiS@NC, except omitting the covering PDA and presintering process.

2.2. Structure characterizations

The scanning electron microscopy (SEM) and transmission electron microscopy (TEM) investigations were performed on JSM-7900F and JEM-F200, respectively. The chemical composition of products was studied by EDX. The crystal structure was recognized by powder XRD with Cu-K_α radiation (Empyrean PANalytical, Holland; λ = 0.154 nm). Raman spectrum of FeCo-NiS@NC was obtained by Renishaw Micro-Raman spectroscopy system (inVia Reflex, Renishaw) with the wavelength of 532 nm. X-ray photoelectron spectroscopy (XPS) was performed to investigate the chemical bonding of samples using the thermo escalab 250Xi system. *In-situ* XRD analysis of FeCo-NiS@NC electrode during the galvanostatic de/lithiation process was tested by Bruker D8 X-ray diffractometer operating with θ–θ scan mode and Cu K_α radiation. An airtight *in-situ* electrochemical cell-equipped using a Be window was galvanostatically charged and discharged at the current rate of 100 mA g^{-1}. In the *in-situ* cell, the homogeneous slurry was directly coated on the Be window with the weight of ∼3.5 m g cm^{-2} to strengthen the intensity of diffraction peaks. Simultaneously, the data were recorded with a scanning speed of 2° min^{-1} in the angular range of 20°–80°. All ^{7}Li NMR experiments were acquired on a Bruker 400 MHz spectrometer (AVANCE HD III) with 4.0 mm HX MAS probe. The Larmor frequency for ^{7}Li was 155.52 MHz. All *ex-situ* electrodes were filled into 4.0 mm rotors inside an argon glovebox. The spinning rate was set to 10 kHz. Single pulse of 1.6 μs was set for 90° to polarize ^{7}Li magnetizations. 1 mol L^{-1} LiCl solution at 0 ppm was set as ^{7}Li shift reference.

2.3. Battery fabrication and electrochemical measurements

FeCo-NiS@NC electrodes were prepared by mixing 70 wt% active materials, 20 wt% acetylene black, and 10 wt% CMC (Carboxymethylcellulose sodium) binder in deionized water. The homogeneous slurry was cast on a copper foil and dried at 120 °C in a vacuum oven for 12 h. The dried electrode was punched into discs in a diameter of 12 mm, converting into 1.131 cm^2. The mass loading of active materials was measured and calculated as around 1.0 mg cm^{-2}. The coin cells (CR2023) were assembled in an argon filled glove box with the counter electrode of metallic Li or Na. All electrochemical tests were carried out on a Lanthe CT2001A/B (Wuhan, China) system. Electrochemical impedance spectroscopy (EIS) and cyclic voltammetry (CV) measurements were obtained on an SP-150 electrochemical workstation (BioLogic, France).

3. Results and discussion

3.1. Structural and component characterization

To obtain the target Fe and Co co-doped NiS with N-based carbon, the routine of FeCo-NiS@NC preparation is clearly designed as shown in Fig. 1(a). Trimetallic PBA precursor was firstly synthesized according to our previous work [40]. Two kinds of cyanide metals (Potassium ferricyanide and Potassium hexacyanocobaltate) and Ni^{2+} were mixed in aqueous solution with sodium citrate as the surface-active agent. After aging, the acquired claybank product is trimetallic Prussian blue analogues (NiCoFe-PBA), which was then coated by PDA to form PBA@PDA, followed by vulcanization and annealing to obtain the final product FeCo-NiS@NC. Their morphologies and structures are tracked by SEM and XRD (Fig. 1b–
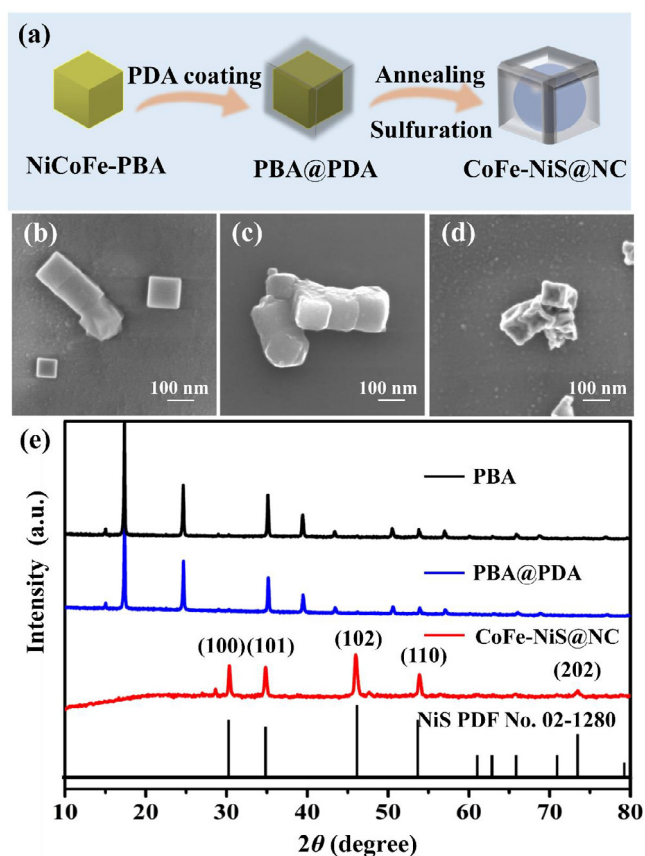
Fig. 1. (a) Schematic illustration of FeCo-NiS@NC fabrication, (b–d) SEM images and (e) XRD patterns of PBA, PBA@PDA, and FeCo-NiS@NC, respectively. The reference of NiS (PDF card no. 02–1280) is shown at bottom.

e). Trimetallic PBA precursor exhibits uniform cubic morphology and smooth surface. The morphology became irregular and formed core-shell particles after coating with PDA. The FeCo-NiS@NC nanocubes reveal the core–shell structure with an average size of ~110 nm, which shows a slight shrink when compared with PBA@PDA, whose size centralizes at ~125 nm as shown in Fig. S1. The average size of PBA is ~105 nm, being smaller than that of PBA@PDA, which is due to the PDA coating layer of about 20 nm in thickness. Energy-dispersive X-ray spectroscopy (EDS) shows that both PBA and PBA@PDA contain elements of C, N, Fe, Co and Ni (Fig. S2). The intensity of C in PBA@PDA is higher than that of PBA because of the PDA coating. The ratios of Co, Fe, Ni and S within PBA, PBA@PDA and FeCo-NiS@NC obtained by EDS were summarized in Table S1. The atomic ratios of FeCo-NiS@NC are strongly determined by its precursor, which means that the metal proportion of PBA precursor could be easily modulated to achieve optimized composition and performance properties. The EDS results indicate that the ratio of Ni/(Co+Fe) decreased from PBA to PBA@PDA, and further for the final product FeCo-NiS@NC, which is likely due to the depth limitation of EDS. The ratio of (Ni+Co+Fe)/S is roughly determined as ~1 for FeCo-NiS@NC, reflecting the replacement of Ni by Fe and Co. In order to further precisely affirm the ratio of the three metal elements, the atomic percentage is trancked by inductively coupled plasma mass spectrometry (ICP-MS). After normalization, the ratios of Ni, Co and Fe is 3.3, 1 and 1.1, respectively (Table S2). The XRD patterns reveal that the PDA coating does not destroy the crystal structure of PBA (Fig. 1e). In addition, the final product FeCo-NiS@NC contains intensive crystalline feature of NiS phase (PDF No. 02–1280), which is quite dif-

ferent from PBA and PBA@PDA precursors. As shown in Fig. 1(e) and Fig. S3, the final product FeCo-NiS@NC is well indexed by the PDF card of NiS, rather than the superposition of NiS, CoS and NiS. The slight shift of XRD pattern is due to the doping of Co and Fe, which lead to the changes of NiS structure.

The detailed structure of FeCo-NiS@NC was further characterized by TEM. As shown in Fig. 2(a), the internal core shrinks and generates obvious voids in the corner. The outer carbon layer displays a thickness of ~10 nm. The Raman spectrum of carbon shell exhibits both D and G bands (Fig. S4), indicating that the PDA coating was successfully calcined into carbon. The D band at around 1350 cm^{-1} represents the breathing mode of sp^2-C atoms and the G band at ~ 1600 cm^{-1} attributes to the bone stretching mode of sp^2 carbons. The intensity ratio of the D band and the G band ($R_{DG} = I_D/I_G$) is often considered as a measure of disordered graphite [33,41–43]. The high value of R_{DG} (close to 1) reflects that the nanoparticle is covered by amorphous carbon, which is consistent with the HRTEM results. In addition, the lattice fringes with d-spacing of 0.257 and 0.196 nm are shown in Fig. 2(b and c) corresponding to the (110) and (102) planes of crystalline NiS obtained from the above XRD study.

EDS mappings shown in Fig. 2(d–j) further consolidate core-shell structure of FeCo-NiS@NC. Elements C and N are found to be uniformly distributed in the outer shell, while Ni, Co, Fe and S are observed within the inside core. Additionally, the EDS linear scan across a single FeCo-NiS@NC nanocube demonstrates high content of Ni, Co, Fe and S in the core with a length of ~70 nm and the C in the shell with a length of ~140 nm (Fig. S5). Moreover, the uniformly distributed elements of Fe, Co and Ni also prove that the PBA precursor completely transferred to Fe/Co-doped NiS and PDA coating turned into hollow C shell after thermal and vulcanization processes. In addition, the EDS spectrum verifies the existence of C, N, Ni, Fe, Co and S elements in FeCo-NiS@NC (Fig. S6). The XRD pattern, SEM image and EDS spectrum of individual FeCo-NiS also be investigated in Figs. S7 and S8. As expected, the XRD curve indicates that FeCo-NiS is indexed to NiS phase (Fig. S7), being the same as FeCo-NiS@NC core. SEM results (Fig. S8) show that the morphology of FeCo-NiS is irregular with a particle size of ~2 μm, which is obviously bigger than that of FeCo-NiS@NC (Fig. 2). This is mainly due to the agglomeration during vulcanization and annealing process without protecting by carbon shell. To further understand the effect of the carbon shell, the Nitrogen adsorption and desorption and thermogravimetric analysis (TGA) are shown in Fig. 2(k and l). Comparing with FeCo-NiS, the FeCo-NiS@NC composites show an obvious hysteresis loop at a high relative pressure (from 0.8 to 1.0), reflecting the presence of more mesopores. The inset suggests that plenty of macropores in the range of 40–70 nm are found for FeCo-NiS, with an average pore size of 51.96 nm in diameter. However, the FeCo-NiS@NC shows both mesopores and macropores in the size between 3 to 110 nm with an average size of 19.46 nm in diameter. Besides, the Brunauer-Emmett-Taller (BET) specific surface areas of FeCo-NiS@NC and FeCo-NiS are identified as 24.5787 and 0.7885 m^2 g^{-1}. Obviously, the N-doped carbon shells significantly increase the specific surface. In the TGA curves, both FeCo-NiS@NC and FeCo-NiS show slight weighty increase between 200 and 450 °C, corresponding to the partial oxidation of metal sulfide to form FeCo-NiSO$_x$. The FeCo-NiS displays more mass increase (6.7%) when compared to the one with carbon shell FeCo-NiS@NC (4.9%). This is due to different degrees of oxidation. Further increasing temperature from 450 to 550 °C, a distinct weight loss occurrs for both materials, which is attributed to two reasons. Firstly, the metal sulfides react with oxygen and decompose to form sulfur oxide gas. About 1.5% is observed for FeCo-NiS decomposition. Secondly, the weight loss is obviously caused by the combustion of carbon shell in the air for FeCo-NiS@NC, and the mass
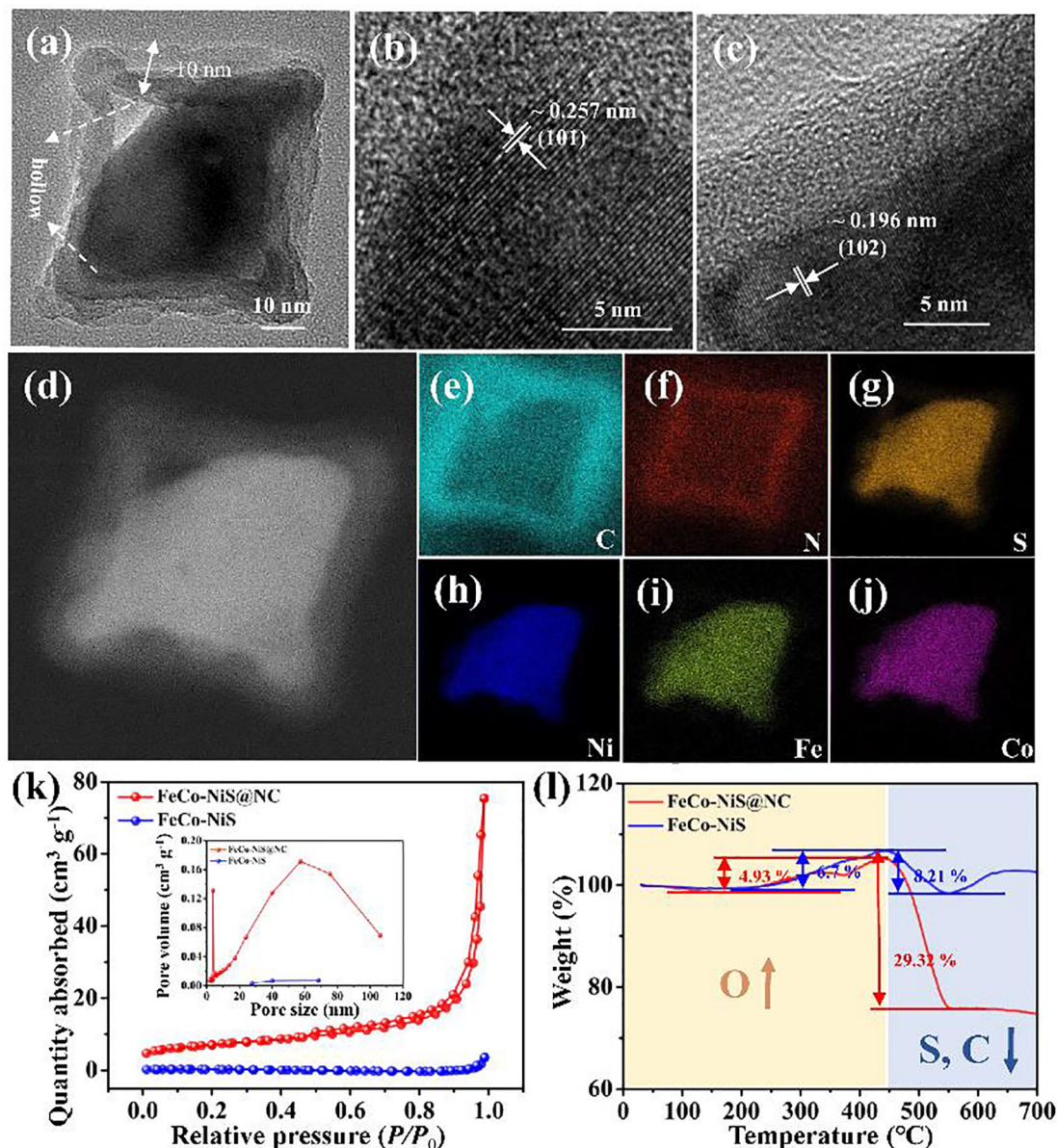
Fig. 2. (a) Low magnification TEM image of FeCo-NiS@NC. (b and c) HRTEM images showing the (101) and (102) planes of the core composite. (d–j) Elemental mapping of the FeCo-NiS@NC: (e and f) C and N in the shell and (g–j) S, Ni, Fe and Co in the core. (k) Nitrogen adsorption and desorption of FeCo-NiS@NC and FeCo-NiS. The inset shows the corresponding pore size distrubutions. (l) TGA curves of FeCo-NiS@NC and FeCo-NiS.

ratio of N-doped carbon shell is roughly calculated as 24.4% (29.3%−4.9%) if the release of sulfur oxide is not taken into account.

The XPS spectrum of all elements in FeCo-NiS@NC is shown in Fig. S9(a). The S $2p$ spectrum (Fig. S9b) displays five peaks at 161.5, 162.7 163.8, 165.7 and 168.4 eV, attributing to S $2p_{1/2}$, sat., S $2p_{3/2}$, sat. and sulphur oxide, respectively [32,44]. The Ni $2p$, Co $2p_{3/2}$ and Fe $2p$ are also plotted in Fig. S9(c). The two strong peaks at around 854.6 and 872.1 eV are assigned to $2p_{1/2}$ and $2p_{3/2}$ of Ni $2p$ in FeCo-NiS@NC [45], with two satellite peaks at 860.9 and 879.7 eV. The only weak broad peak at 780.7 eV corresponds to Co $2p_{3/2}$, which is possibly due to the trace amount of Co on the surface of FeCo-NiS@NC. The two intensive peaks at 711.1 and 724.4 eV are from Fe $2p_{3/2}$ and Fe $2p_{1/2}$ [44]. Fig. S10 presents the XPS analysis of the shell. The N $1s$ spectrum (Fig. S10a) suggests that three peaks at 398.2, 398.9 and 400.4 eV could be allocated to the Pyridine N, Pyrrolic N and Graphitic N, respectively [16]. The C $1s$ spectrum (Fig. S10b) shows three peaks at 284.8, 285.9 and 289.2 eV, being attributed to C–C, C–N and C=N species [20]. More-

over, the C–N and C=N species may originate from the PDA coating layer. After high temperature treatment, the PDA at surface carbonized to form N doped amorphous carbon. The graphitic N is considered to promote electron transport through carbon shell, which is beneficial to fast rate performance. The pyridinic and pyrrolic-N could be used to offer extra capacity via pseudocapacitive mechanism [46].

3.2. Electrochemical performance for lithium- and sodium- ion batteries

The electrochemical performance of the FeCo-NiS@NC anode for lithium-ion batteries was tested by CV at a scan rate of 0.2 mV s^{-1} (Fig. 3). In the first cathodic scan, an asymmetric peak appearing between 0.77 and 1.5 V is likely to contain two merged peaks. This irreversible cathodic peak (current maxima at ∼0.98 V) is possibly raised by the decomposition of electrolyte to form solid electrolyte interface (SEI) film and irreversible Li$^+$ storage in the electrode
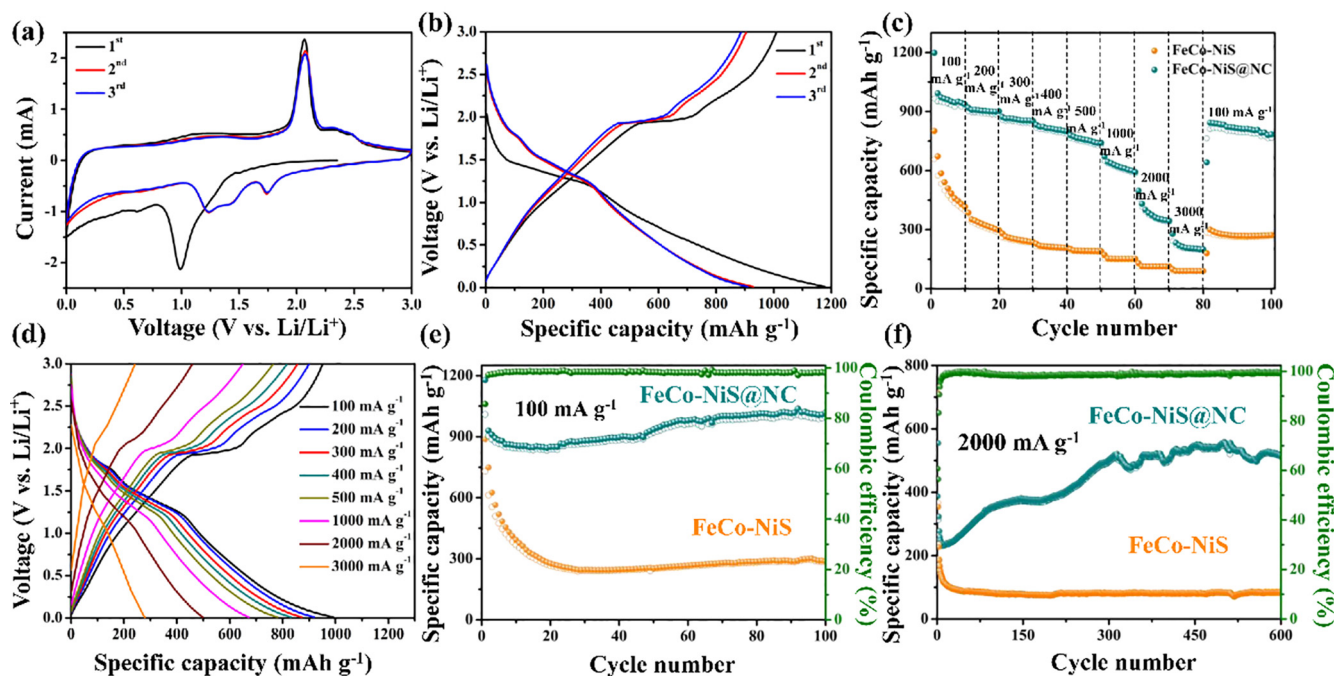
Fig. 3. Electrochemical performance of FeCo-NiS@NC in a lithium half-cell. (a) CV curves of FeCo-NiS@NC electrode in the initial three cycles with the scan rate of 0.2 mV s^{-1}. (b) Galvanostatic de/lithiation voltage profiles of the first three cycles at the specific current of 100 mA g^{-1}. (c) Rate performance of FeCo-NiS@NC and FeCo-NiS. (d) The corresponding charge/discharge curves of FeCo-NiS@NC at different current densities. (e) Cycle performances of FeCo-NiS@NC and FeCo-NiS at 100 mA g^{-1}. The discharge and charge processes were marked by solid cycles and hollow cycles, respectively. (f) Long-term cycle performance of FeCo-NiS@NC and FeCo-NiS at a current density of 2000 mA g^{-1}.

[47,48]. In the first anodic scan, the broad peak at 1.22 V is attributed to the partial decomposition of SEI film. The next peaks at 2.07, 2.32 and 2.47 V are assigned to the conversion of metal to form metal sulphides. According to previous studies [16,49,50], the two oxidation peaks of Ni, Co and Fe are similarly shown at $\sim$2.0 and 2.4 V, respectively. So the shoulder peaks at 2.32 V and 2.47 V are attributed to the doping effects of Fe and Co, which increase the number of reacting Li$^+$. In the second cycle, the cathodic scan exhibits three peaks at 1.73, 1.40 and 1.23 V, which are due to three kinds of Li$^+$ storage steps into the rearranged active material according to the slightly different standard potential of Ni^{2+}, Co^{2+} and Fe^{2+} when paired with their metallic elements. The second anodic scan is almost identical to the first anodic scan, except a slight intensity drop is observed for the peak at 2.07 V because of the irreversible reaction. The third scan totally overlaps with the second one, revealing excellent reversibility of FeCo-NiS@NC electrode. Fig. 3(b) shows the galvanostatic cycling of FeCo-NiS@NC electrode during the initial three cycles. In the 1st cycle, the discharge and charge capacities are determined as 1178.9 and 1009.7 mAh g^{-1}, respectively. It is worth noting that the FeCo-NiS@NC electrode shows outstanding electrochemical property with the initial Coulombic efficiency (CE) of 85%, which means that only a small amount of Li$^+$ is involved in the formation of SEI. Surprisingly, the CE reaches 97.5 % after three cycles.

The rate performance of FeCo-NiS and FeCo-NiS@NC was compared under various current densities ranging from 100 to 3000 mAh g^{-1} (Fig. 3c), together with cycling curves of FeCo-NiS@NC shown in Fig. 3(d). It is shown that FeCo-NiS@NC demonstrates better rate capability alongside all the applied current densities. Capacities of 900 and 800 mAh g^{-1} can be obtained for FeCo-NiS@NC at current densities of 200 and 500 mA g^{-1}, respectively. However, the capacity of FeCo-NiS drops to 300 mAh g^{-1} at a current density of 200 mA g^{-1}. Surprisingly, a capacity of $\sim$200 mAh g^{-1} is still maintained for FeCo-NiS@NC at a current density of 3000 mA g^{-1}. In addition, FeCo-NiS@NC shows an outstanding

reversible capacity compared to FeCo-NiS: a capacity of $\sim$1000 mAh g^{-1} is achieved for FeCo-NiS@NC when the subsequent current density is set back to 100 mA g^{-1}, but only $\sim$300 mAh g^{-1} is determined for FeCo-NiS. As shown in Fig. 3(e), long cycle life and excellent Coulombic efficiency are observed for FeCo-NiS@NC at a current density of 100 mA g^{-1}, but not for FeCo-NiS. The coulumbic efficiency of FeCo-NiS is shown in Fig. S11. After 20 cycles, the CE of FeCo-NiS is only 96%, but 98.7% of CE is achieved for FeCo-NiS@NC electrode. Long-term performance at high current is also tested, Fig. 3(f) indicates that the FeCo-NiS@NC maintains a considerable capacity of 514 mAh g^{-1} at a current density of 2000 mA g^{-1} after 600 cycles, which has exceeded most electrode materials according to previous reports [47,48,51–54]. However, the FeCo-NiS without carbon nanocubes shows only $\sim$90 mAh g^{-1} from the 20th to 600th cycle. The initial electrochemical cycling performance of FeCo-NiS is shown in Fig. S12. It is obvious to observe that the capacity of FeCo-NiS decays intensively upon cycling because of structural instability, such as particle fracture inside metal sulphides. To overcome this challenging issue, coating with N-doped carbon shell can effectively buffer the volume change and thus stabilize the core structure during charge/discharge process [12,55–58]. Moreover, the capacity of FeCo-NiS is obviously lower than that of FeCo-NiS@NC electrode. In addition, the carbon coating layer can enhance electronic conductivity for fast cycling as well. Fig. S12(c) compares the EIS of FeCo-NiS and FeCo-NiS@NC. The semicircle at high-frequency region is ascribed to the charge transfer resistance (R_{ct}) and the inclined line at low-frequency field is often correlated to the Warburg impedance (Z_w) of Li$^+$ diffusion. The EIS curves obviously demonstrate that the existence of carbon shell promotes electronic conductivity significantly [12,21,59,60]. In short, the proposed Fe and Co co-doped FeCo-NiS@NC shows excellent properties in terms of capacity, stability and rate performance. To our best knowledge, it demonstrates obvious superiority when compared to the ever reported NiS electrodes as listed in Table S3.

To futher understand the doping effect of Fe and Co, pure NiS was prepared [61]. The EDS and atomic ratio indicate that the NiS is synthesized successfully (Fig. S13 and Table S4). The CV at a scan rate of 0.1 mV s^{-1} of NiS is shown in Fig. S14(a). In the first cathodic scan, the peak at 1.71 V corresponds to the lithiation process of NiS [53], the subsequent irreversible broad peak at 1.36 V is assigned to the generation of Ni. The peak at 0.58 V is attributed to the formation of solid electrolyte interface, which is also comfirmed by its disappearance in the subsequent cycles [62]. In the first anodic scan, two peaks at 1.36 and 2.12 V are assigned to the formation of metal sulphides. The intensity of all peaks decreases distinctly during the second and the thrid cycles caused by the reversibility. In addition, the capacity of NiS decays during the first three cycles. The discharge and charge capacities in the 1st cycle are 296 and 695 mAh g^{-1}, respectively (Fig. S14b). The capacities of pure NiS are inferior to these of FeCo-NiS and FeCo-NiS@NC. Additionally, the R_{ct} of NiS is also larger than that of the FeCo-NiS@NC electrode (Fig. S14c), indicating that doping and covering with carbon could efficiently enhance the electronic conductivity.

To further investigate the kinetics of FeCo-NiS@NC composite, CV was performed by applying different scan rates ranging from 0.2 to 2.0 mV s^{-1} (Fig. 4). Multiple peaks are detected in the CV curves due to different redox potential of various doped metal elements. These peaks show a slight shift evolution upon changing scan rate. According to Dunn [43,63,64], the effect of pseudo-capacitance could be calculated by confirming the relationship of peak current (i) and the scan rate (v) on the basis of the following equations:.

$$i = a v^b \tag{1}$$

$$\log(i) = b \times \log(v) + \log(a) \tag{2}$$

In these equations, a is constant, and b value is determined by $\log(i)$ and $\log(v)$. When b value is close to 1, the surface capacitive process dominates the electrochemical reactions; and if b value is close to 0.5, the diffusion-controlled process plays a major role. In Fig. 4(a and b), four main peaks were chosen to analyze, and b values of different redox states are determined as 0.62, 0.84, 0.88 and 0.78, respectively. This suggests that both diffusion charge storage and pseudo-capacitance behaviors address the electrochemical reaction process. The proportion of pseudo-capacitance and diffusion mechanisms can be further quantified according to the following equations:

$$i(V) = k_1 v + k_2 v^{1/2} \tag{3}$$

$$i/v^{\frac{1}{2}} = k_1 v^{1/2} + k_2 \tag{4}$$

where k_1 and k_2 are constants at a given potential. In Equation (3), $k_1 v$ represents the capacitive contribution and $k_2 v^{1/2}$ is controlled by diffusion. Equation (4) is derived from Equation (3), and k_1 value corresponds to the slope of $i/v^{1/2}$ and $v^{1/2}$, the k_2 represents the intercept. The pseudo-capacitance contributes 61.9% for FeCo-NiS@NC at a scan rate of 0.2 mV s^{-1} (Fig. 4c and d). With the raising of scan rate, the capacitive contribution increases to 64.2%, 67.7%, 72.1%, 78.7% and 83.7%, respectively (Fig. 4d). The statistical results demonstrate that the capacitive contribution offers the primary reversible capacity (Fig. 4d). The kinetic analysis of FeCo-NiS with lithium storage also be tested in Fig. S15. As shown in Fig. S15(a), the CV was performed by various rate from 0.2 to 1.0 mV s^{-1}. And the b values of the two main peaks are 0.6 and 0.58. The capacitive contribution at different scan rates is exhibited in Fig. S15(c).
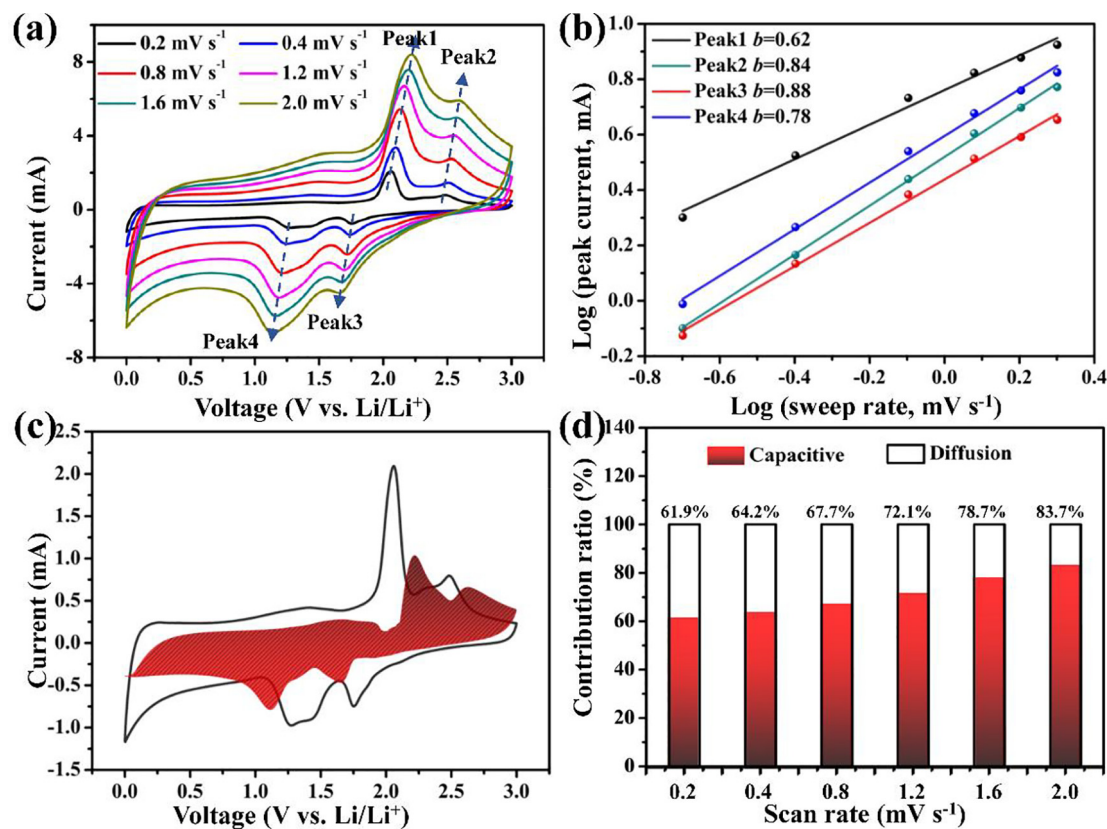

Fig. 4. Kinetic analysis of the lithium storage for FeCo-NiS@NC anode. (a) CV curves of FeCo-NiS@NC electrode at various scan rates. (b) Calculation of b value by using the correlation of sweep rate and peak current. (c) Determination of capacitive and diffusion-control current in overall cyclic voltammogram of FeCo-NiS@NC electrode with a scan rate of 0.2 mV s^{-1} shown by the shaded region. (d) The percentages of capacitive and diffusion contribution to the overall capacity.
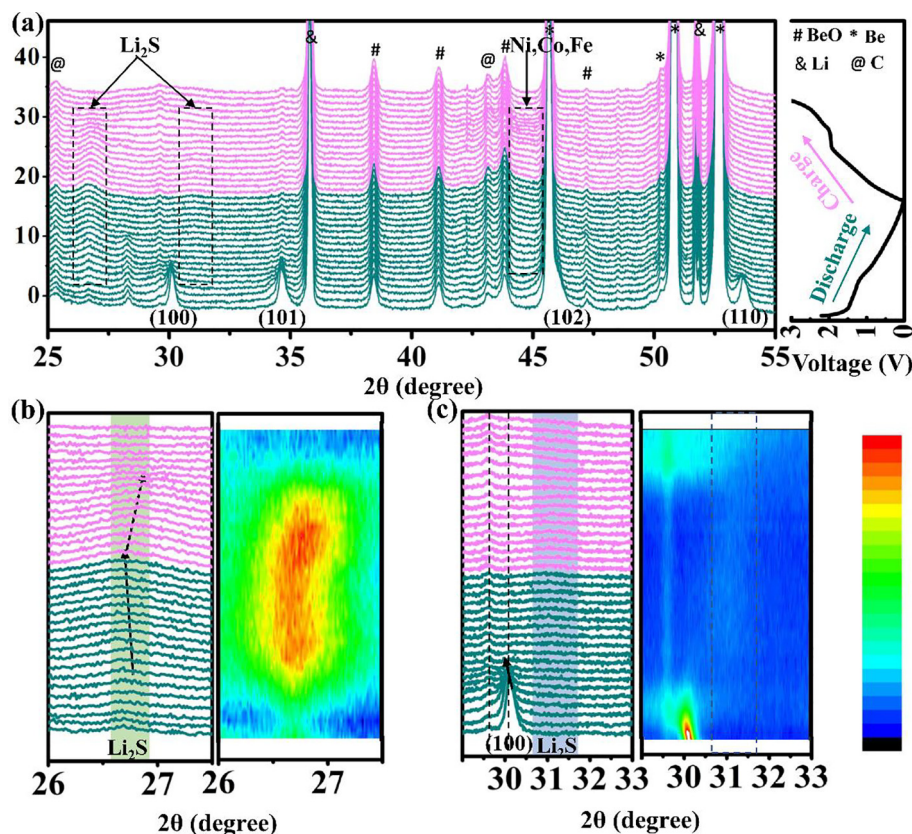
Fig. 5. (a) *In-situ* XRD of FeCo-NiS@NC electrode during the 1st de/lithiation process. The cycling curve is presented to the right. (b) and (c) Enlargement of the selected regions. XRD patterns are displayed on the left panel and the contour plots are shown on the right panel.

With the raising of scan rate from 0.2 to 1.0 mV s^{-1}, the capacitive contribution increases from 31.6% and 59.6%. This values is obviously lower than that of FeCo-NiS@NC anode.

To check the feasibility of the obtained FeCo-NiS@NC, half-cells coupled with sodium metal are also evaluated in Fig. S16. Fig. S16 (a) displays typical CV curves of the initial three cycles with a scan rate of 0.2 mV s^{-1}. In the 1st cathodic scan, three obvious irreversible peaks are detected at the voltages of 0.1, 0.6 and 0.8 V (vs. Na/Na$^+$), which is lower than that of LIBs as expected. Three reduction peaks are found during the SEI formation due to multiple metals doping. In the 1st anodic scan, the small peak at 0.98 V is identified as partial decomposition of SEI film, and the following peak at 1.81 V corresponds to the resulphidation process of metals (Fe, Co and Ni). After the 1st activate cycling process, the structure is rearranged, and three new peaks appear during the 2nd cathodic scan due to three distinct Na$^+$ intercalations. The 3rd cycle is almost identical to the 2nd charge-discharge process. As shown in Fig. S15(b), capacities of 699.7 and 577.8 mAh g^{-1} are respectively obtained for the 1st discharge and charge process. The reversible capacities of the following 2nd and 3rd cycles are ~600 mAh g^{-1}. The rate performance and cycling stability are shown in Fig. S16(c and d). Accordingly, the FeCo-NiS@NC electrodes were tested by galvanostatic cycling under various current densities from 100 to 1000 mA g^{-1}, and the average specific capacities are determined as 538, 497, 457, 403, 346 and 294 mAh g^{-1}, respectively. When the current density was set back to 100 mA g^{-1}, the average specific capacity recovers to be 473 mAh g^{-1}, which means good capacity retention of 88%. In addition, Fig. S15(d) indicates good cycling stability of FeCo-NiS@NC electrode, which offers a specific capacity of 453.6 mAh g^{-1} after 100 cycles at a current density of 100 mA g^{-1}. In short, the FeCo-NiS@NC can serve as Na$^+$ anode with good performance for SIBs.

3.3. XRD and NMR characterizations of reaction mechanisms

To further investigate the insertion and extraction reactions of FeCo-NiS@NC anode during electrochemical cycling, XRD and NMR were performed during the first charge and discharge at a current density of 100 mA g^{-1} for LIBs. As *in-situ* XRD displayed in Fig. 5, the pristine FeCo-NiS@NC electrode (scan 1 in Fig. 5a) mainly shows three characteristic peaks of NiS at 30.1°, 34.6° and 53.6°, respectively. Upon the 1st discharge, the XRD pattern of FeCo-NiS@NC slightly moves to low angle (scan 1 to 2 in Fig. 5a and c) during the voltage from 2.25 to ~1.52 V with the unconspicuous increase of capacity. This phenomenon may attribute to the absorption of Li$^+$ and a few redox reactions happening at the surface. Then, the active materials at surface transferres to Li$_x$FeCo-NiS@NC and the inner part retains the structure of NiS, which leads to the splitting peaks in the contour plot (scan 2 to 6 in Fig. 5c). In this stage, the capacity increases obviously, which is assigned as pseudo-capacitance-controlled process as afore discussed. Upon further discharge, the intensities of peaks at 30.1°, 34.6° and 53.6° decline until they completely disappear (scan 6 to 10). Meanwhile, a broad peak at 26.7° grows due to the formation of Li$_2$S (111) (Fig. 5b) and possible metallic Ni, Co and Fe (Fig. S17) [43]. As shown in Fig. 5(b), the peak of Li$_2$S moves to low angle during discharge process. This may be explained as the initial formation of a small amount of Li$_2$S would be affected by the stress of the surrounding environment. Upon subsequent charge, Li$^+$ is gradually extracted from active electrode and the intensity of Li$_2$S thus decreases and moves to high angle. When the voltage reaches ~2.0 V, the phase of Li$_x$FeCo-NiS@NC reappeares and coexists with Li$_2$S. Finally, the Li$_2$S converts to Li$_x$FeCo-NiS@NC at the end of one cycle. The broad signals at ~30° and 53° show up during charge process are due to the increase of disordering upon electrochemi-

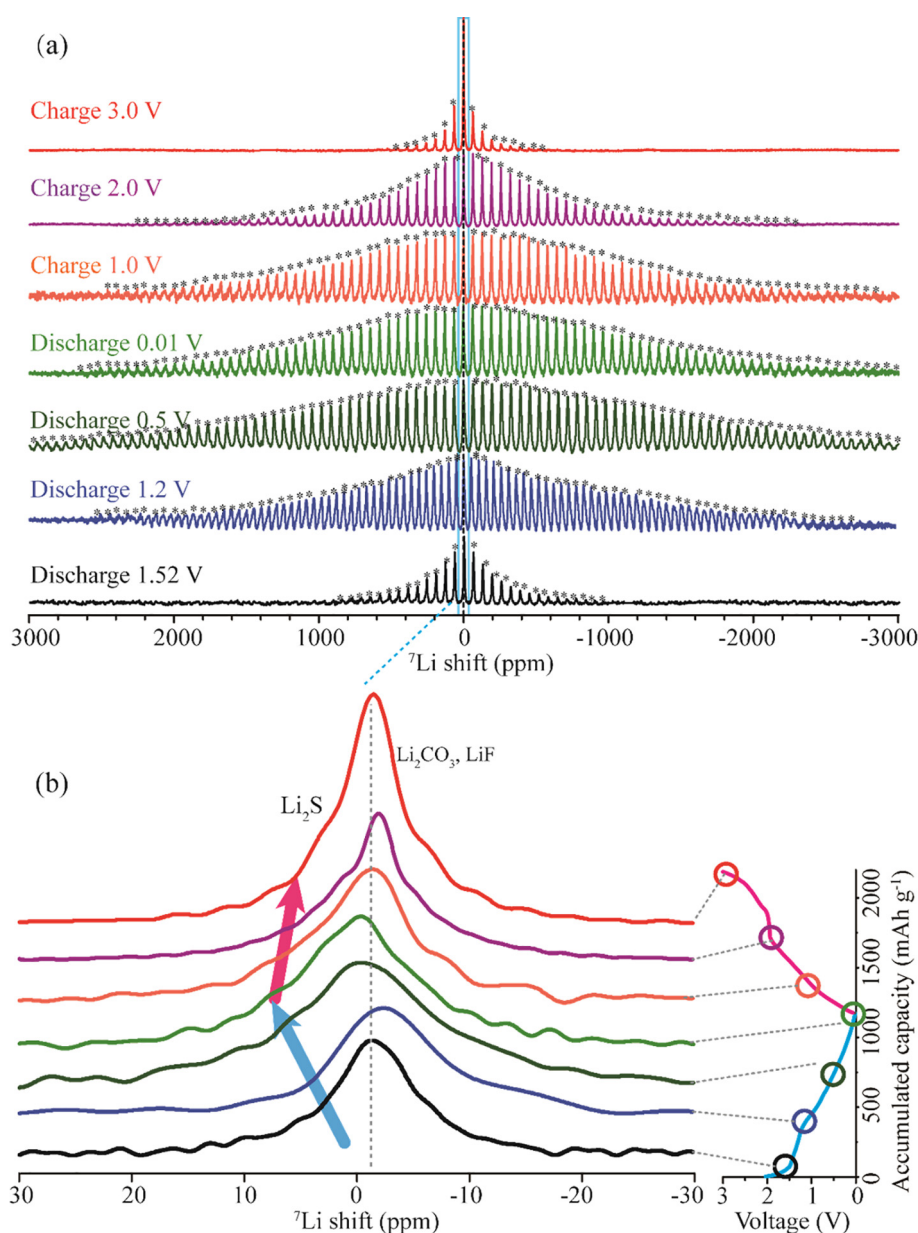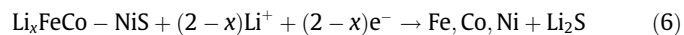**Fig. 6.** (a) Solid-state ^7Li NMR spectra for FeCo-NiS@NC electrodes at various charge-discharged states, with the isotropic peaks shown in (b). The electrochemical curve is plotted on the right of (b). SSBs are marked with asterisks.

cal cycling. Claimed by other literatures, NiS tends to transfer to Ni_3S_2 and lose some S after the first cycle [47,62,65], resulting in capacity decay. However, this is not observed for the FeCo-NiS@NC, reflecting that Fe, Co doping and C coating play a key role in stabilizing structure.

NMR spectroscopy has been proved as a suitable tool to investigate the local structure at atomic level for materials [66–68]. Solid-state ^7Li NMR spectra were measured and analyzed for the cycled LixFeCo-NiS@NC electrodes obtained at various states of lithiation as shown in Fig. 6. Magic angle spinning rates of 8 and 10 kHz were performed to distinguish the isotropic peak and spinning sidebands (SSBs) as shown in Fig. S18. All the FeCo-NiS@NC electrodes show an isotropic signal centered at ~0 ppm with multiple SSBs (Fig. 6a). The electrode discharged to 1.52 V displays a large anisotropy of ~2000 ppm accounting for all SSBs, possibly due to intensive anisotropy of Li and strong electron-nuclear dipolar coupling raised by the unpaired electron coming from metallic

elements (Fe, Co and Ni) or a broad environment distribution induced by sub-domain or the 2nd and the 3rd coordination shells [69]. When the electrode is further discharged to 1.2 V, the order of SSBs increases and the full spectrum spreads up to 4000 ppm. The spectra become even broader upon deeper lithiation as the samples discharged to 0.5 and 0.01 V with increased intensity. A reverse trend is observed for these spectra upon subsequent charge. The electrode after one cycle (charge to 3.0 V) shows a sharp intensive isotropic peak with only ~1500 ppm width of SSBs, which is possibly caused by incomplete capacity recovery, such as SEI film. For more clear discussion, the isotropic resonances are enlarged and shown in Fig. 6(b). All spectra localized near 0 ppm, indicating the formation of Li_2S [70,71]. Upon discharge, the amount of Li_2S increases due to the lithiation into the anode. The isotropic linewidth grows, and the peak position seems to shift towards downfield, which is possibly due to the change of redox states and the formation of metallic Fe, Co and Ni, resulting in

Knight shift effect. Reversible trends are observed for the anode when it experiences subsequent delithiation process. For the sample after one cycle, the central sharp peak becomes more obvious, which is mainly originated from the irreversible intercalated Li and the SEI components, such as LiF and Li_2CO_3 [72]. In sum, the NMR results are clearly the evolution behind electrochemical cycling and are in good agreement with the afore-mentioned XRD study. Therefore, the chemical formulas of lithiation can be summarized as below.

$$FeCo - NiS + xLi^+ + xe^- \rightarrow Li_xFeCo - NiS \qquad (5)$$

$$Li_xFeCo - NiS + (2-x)Li^+ + (2-x)e^- \rightarrow Fe, Co, Ni + Li_2S \qquad (6)$$

The microscopy images of FeCo-NiS@NC electrode after lithiation are shown in Fig. S19. The morpphology of the active materials preserves cubic core–shell structure (Fig. S19a). The low magnification TEM image shows that the FeCo-NiS@NC goes through volume expansion compared with the initial materials (Fig. 2a) and breaks up into small particles (Fig. S19b). However, all FeCo-NiS particles are well protected by the carbon nonacubes. The electrode after 500 cycles at a current density of 2000 mA g^{-1} was also tested by SEM and TEM in Figs. S20 and S21. The SEM image shows that the morphology of active materials becomes irregular but it still maintains the core–shell configuration. The high-resolution TEM indicates that the d-spacing of 0.31 nm increases distinctly for the core FeCo-NiS particles (Fig. S21). In sum, the core–shell structure is well maintained after charge–discharge cycling.

4. Conclusions

Multiple metals (Fe, Co, Ni) modulated sulfide with the substrate of PBA precursor was carefully designed and served as anodes for both lithium- and sodium- ion batteries. The excellent electrochemical performances of the obtained anodes are attributed to the following merits: (a) the N-doped carbon shell not only provides high electronic conductivity but also retains the nanometer size and cubic morphology to shorten the transport path of alkali metal ions and electrons; (b) the core–shell structure effectively prevents the agglomeration of the active core electrode and the hollow space between core and shell greatly buffers the volume change during intercalation and extraction processes, and (c) the ratio of metal elements can be adjusted in the Prussian blue analogue precursor to modulate the capacity and potential of the final anode. Electrochemical investigations reveal that the capacity is mainly manipulated by a pseudo-capacitance process. XRD and NMR results demonstrate that the conversion reaction mechanism is mainly addressed. The proposed strategy for multimetal doping with the aid of Prussian blue analogue opens a way of designing electrodes with enhanced stability, reversible capacity and rate performance.

Declaration of competing interest

The authors declare that they have no known competing financial interests or personal relationships that could have appeared to influence the work reported in this paper.

Acknowledgments

Appendix A. Supplementary data

Supplementary data to this article can be found online at https://doi.org/10.1016/j.jechem.2022.02.053.

References

[1] F. Wu, J. Maier, Y. Yu, Chem. Soc. Rev. 49 (2020) 1569–1614.
[2] H. Cheng, J.G. Shapter, Y. Li, G. Gao, J. Energy Chem. 57 (2021) 451–468.
[3] Z. Zheng, P. Li, J. Huang, H. Liu, Y. Zao, Z. Hu, L. Zhang, H. Chen, M.-S. Wang, D.-L. Peng, Q. Zhang, J. Energy Chem. 41 (2020) 126–134.
[4] S. Fang, D. Bresser, S. Passerini, Adv. Energy Mater. 10 (2019) 1902485.
[5] E. Goikolea, V. Palomares, S. Wang, I.R. Larramendi, X. Guo, G. Wang, T. Rojo, Adv. Energy Mater. 10 (2020) 2002055.
[6] A. Wang, W. Hong, L. Yang, Y. Tian, X. Qiu, G. Zou, H. Hou, X. Ji, Small 16 (2020) 2004022.
[7] M.R. Palacin, Chem. Soc. Rev. 38 (2009) 2565–2575.
[8] L. Chen, X. He, H. Chen, S. Huang, M. Wei, J. Mater. Chem. A 9 (2021) 22048–22055.
[9] J. Jang, J.H. Ku, S.M. Oh, T. Yoon, ACS Appl. Mater. Interfaces 13 (2021) 9814–9819.
[10] A. Raza, J.Y. Jung, C.H. Lee, B.G. Kim, J.H. Choi, M.S. Park, S.M. Lee, ACS Appl. Mater. Inter. 13 (2021) 7161–7170.
[11] Z. Liu, M. Yu, X. Wang, F. Lai, C. Wang, N. Yu, H. Sun, B. Geng, Chem. Commun. 57 (2021) 1786–1789.
[12] Q. Li, Y. Wang, Q. Tan, Z. Zhong, F. Su, Chem.-Eur. J. 26 (2020) 12882–12890.
[13] J.H. Chang, J.Y. Cheong, Y. Shim, J.Y. Park, S.J. Kim, J. Lee, H.J. Lee, H. Lim, W. Liu, Q. Zhang, T. Osamu, C.-W. Lee, I.-D. Kim, J. Yuk, J. Mater. Chem. A 9 (2021) 6242–6251.
[14] X. Li, S. You, J. Du, Y. Dai, H. Chen, Z. Cai, N. Ren, J. Zou, J. Mater. Chem. A 7 (2019) 25853–25864.
[15] C.C. Li, B. Wang, D. Chen, L.-Y. Gan, Y. Feng, Y. Zhang, Y. Yang, H. Geng, X. Rui, Y. Yu, ACS Nano 14 (2019) 531–540.
[16] L. Yao, Q. Gu, X. Yu, ACS Nano 15 (2021) 3228–3240.
[17] S. Zhang, H. Ying, P. Huang, J. Wang, Z. Zhang, T. Yang, W.Q. Han, ACS Nano 14 (2020) 17665–17674.
[18] S.H. Yu, M.J. Zachman, K. Kang, H. Gao, X. Huang, F.J. DiSalvo, J. Park, L.F. Kourkoutis, H.D. Abruña, Adv. Energy Mater. 9 (2019) 1902773.
[19] Z. Chen, S. Li, Y. Zhao, M.F. Aly Aboud, I. Shakir, Y. Xu, J. Mater. Chem. A 7 (2019) 26342–26350.
[20] J. Chu, Q. Yu, K. Han, L. Xing, C. Gu, Y. Li, Y. Bao, W. Wang, J. Mater. Chem. A 8 (2020) 23983–23993.
[21] L. Chen, N. Luo, S. Huang, Y. Li, M. Wei, Chem Commun (Camb) 56 (2020) 3951–3954.
[22] L. Chen, W. Yang, X. Li, L. Han, M. Wei, J. Mater. Chem. A 7 (2019) 10331–10337.
[23] X. Li, X. Wang, X. Yang, Z. Zhu, R. Zhao, Q. Li, J. Xu, G. Zhao, H. Li, S. Li, A.C. S. Appl, Mater. Interfaces 11 (2019) 39961–39969.
[24] W. Liu, X. Yuan, X. Yu, ACS Appl Mater. Interfaces 13 (2021) 12016–12021.
[25] X. Wang, K. Chen, G. Wang, X. Liu, H. Wang, ACS Nano 11 (2017) 11602–11616.
[26] K.H. Kim, S.H. Hong, Adv. Energy Mater. 11 (2021) 2003609.
[27] R. Tian, A. Griffin, M. McCrystall, M. Breshears, A. Harvey, C. Gabbett, D.V. Horváth, C. Backes, Y. Jing, T. Heine, S.H. Park, J. Coelho, V. Nicolosi, M. Nentwig, C. Benndorf, O. Oeckler, J.N. Coleman, Adv. Energy Mater. 11 (2020) 2002364.
[28] Z. Liu, S. Yang, B. Sun, P. Yang, J. Zheng, X. Li, Angew. Chem., Int. Ed. Engl. 59 (2019) 1975–1979.
[29] H. Dai, M. Tang, J. Huang, Z. Wang, ACS Appl. Mater Interfaces 13 (2021) 10870–10877.
[30] J. Huang, Z. Wei, J. Liao, W. Ni, C. Wang, J. Ma, J. Energy Chem. 33 (2019) 100–124.
[31] A. Abdul Razzaq, X. Yuan, Y. Chen, J. Hu, Q. Mu, Y. Ma, X. Zhao, L. Miao, J.-H. Ahn, Y. Peng, Z. Deng, J. Mater. Chem. A 8 (2020) 1298–1306.
[32] R. Zang, P. Li, X. Guo, Z. Man, S. Zhang, C. Wang, G. Wang, J. Mater. Chem. A 7 (2019) 14051–14059.
[33] Q. Liu, S.J. Zhang, C.C. Xiang, C.X. Luo, P.F. Zhang, C.G. Shi, Y. Zhou, J.T. Li, L. Huang, S.G. Sun, ACS Appl. Mater. Interfaces 12 (2020) 43624–43633.
[34] P. Wang, M. Shen, H. Zhou, C. Meng, A. Yuan, Small 15 (2019) 1903522.
[35] X.D. Lou, Angew. Chem. Int. Ed. Engl. 132 (2019) 2666–2670.
[36] N.M. Santhosh, N. Shaji, P. Stražar, G. Filipič, J. Zavašnik, C.W. Ho, M. Nanthagopal, C.W. Lee, U. Cvelbar, J. Energy Chem. 67 (2022) 8–18.
[37] T. Xing, Y. Ouyang, L. Zheng, X. Wang, H. Liu, M. Chen, R. Yu, X. Wang, C. Wu, J. Energy Chem. 42 (2020) 108–115.
[38] F. Yang, S. Wang, J. Guan, L. Shao, X. Shi, J. Cai, Z. Sun, J. Mater. Chem. A 9 (2021) 27072–27083.
[39] X. Hu, Y. Liu, J. Li, G. Wang, J. Chen, G. Zhong, H. Zhan, Z. Wen, Adv. Funct. Mater. 30 (2019) 1907677.
[40] J. Liu, S. Wei, N. Li, L. Zhang, X. Cui, Electrochim. Acta 299 (2019) 575–581.
[41] G. Jiao, Y. Gu, J. Wang, D. Wu, S. Tao, S. Chu, Y. Liu, B. Qian, W. Chu, J. Mater. Sci. 54 (2018) 3273–3283.
[42] J.-C. Zheng, Y.-Y. Yao, G.-Q. Mao, H.-Z. Chen, H. Li, L. Cao, X. Ou, W.-J. Yu, Z.-Y. Ding, H. Tong, J. Mater. Chem. A 7 (2019) 16479–16487.
[43] X.M. Lin, J.H. Chen, J.J. Fan, Y. Ma, P. Radjenovic, Q.C. Xu, L. Huang, S. Passerini, Z.Q. Tian, J.F. Li, Adv. Energy Mater. 9 (2019) 1902312.

[44] K. Han, F. An, Q. Wan, L. Xing, L. Wang, Q. Liu, W.A. Wang, Y. Liu, P. Li, X. Qu, Small 17 (2021) 2006719.

[45] X. Wu, S. Li, Y. Xu, B. Wang, J. Liu, M. Yu, Chem. Eng. J. 356 (2019) 245–254.

[46] H. Xu, L. Zhao, X. Liu, Q. Huang, Y. Wang, C. Hou, Y. Hou, J. Wang, F. Dang, J. Zhang, Adv. Funct. Mater. 30 (2020) 2006188.

[47] X. Dong, Z.-P. Deng, L.-H. Huo, X.-F. Zhang, S. Gao, J. Alloy. Compd. 788 (2019) 984–992.

[48] D. Han, N. Xiao, B. Liu, G. Song, J. Ding, Mater. Lett. 196 (2017) 119–122.

[49] M. Yousaf, Z. Wang, Y. Wang, Y. Chen, U. Ali, M. Maqbool, A. Imran, N. Mahmood, P. Gao, R.P.S. Han, Small 16 (2020) 2002200.

[50] X. Wu, S. Li, B. Wang, J. Liu, M. Yu, Chem. Commun. 57 (2020) 1002–1005.

[51] Q. Li, L. Li, P. Wu, N. Xu, L. Wang, M. Li, A. Dai, K. Amine, L. Mai, J. Lu, Adv. Energy Mater. 9 (2019) 1901153.

[52] Y.J. Lee, T.H. Ha, G.B. Cho, K.W. Kim, J.H. Ahn, K.K. Cho, J Nanosci Nanotechnol 20 (2020) 6782–6787.

[53] M. Vadivazhagan, N.K. Shakkeel, K. Nallathamby, Energy & Fuels 35 (2021) 8991–9000.

[54] G. Xia, X. Li, J. He, Y. Wang, Y. Gu, L. Liu, J. Huang, P. Dong, J. Duan, D. Wang, Y. Zhang, Y. Zhang, Ceram. Internat. 47 (2021) 20948–20955.

[55] X. Ma, X. Xiong, P. Zou, W. Liu, F. Wang, L. Liang, Y. Liu, C. Yuan, Z. Lin, Small 15 (2019) e1903259.

[56] Y. Yi, W. Zhao, Z. Zeng, C. Wei, C. Lu, Y. Shao, W. Guo, S. Dou, J. Sun, Small 16 (2020) e1906566.

[57] D. Xie, X. Xia, Y. Zhong, Y. Wang, D. Wang, X. Wang, J. Tu, Adv. Energy Mater. 7 (2017) 1601804.

[58] F. Xiao, X. Yang, D. Wang, H. Wang, D.Y.W. Yu, A.L. Rogach, ACS Appl. Mater. Inter. 12 (2020) 12809–12820.

[59] H. Wu, G. Li, Y. Li, Z. Geng, T. Ren, T. Cai, Z. Yang, Cryst. Res. Technol. 54 (2019) 1800281–1800285.

[60] C. Hu, K. Ma, Y. Hu, A. Chen, P. Saha, H. Jiang, C. Li, Green Energy Environ. 193 (2020) 75–82.

[61] L.Y.X.Y. Yu, H.B. Wu, X.W. Lou, Angew. Chem. Int. Ed. 127 (2015) 5421–5425.

[62] L. Zhang, Y. Huang, Y. Zhang, H. Gu, W. Fan, T. Liu, Adv. Mater. Interfaces 3 (2016) 1500467.

[63] V. Augustyn, J. Come, M.A. Lowe, J.W. Kim, P.L. Taberna, S.H. Tolbert, H.D. Abruna, P. Simon, B. Dunn, Nat. Mater. 12 (2013) 518–522.

[64] G.A. Muller, J.B. Cook, H.S. Kim, S.H. Tolbert, B. Dunn, Nano Lett. 15 (2015) 1911–1917.

[65] H. Geng, S.F. Kong, Y. Wang, J. Mater. Chem. A 2 (2014) 15152–15158.

[66] Y. Shi, M. Tang, Acta Phys. -Chim. Sin. 36 (2020) 1905004.

[67] J. Zheng, M. Tang, Y.Y. Hu, Angew. Chem. Int. Ed. Engl. 55 (2016) 12538–12542.

[68] M. Tang, V. Sarou-Kanian, P. Melin, J.B. Leriche, M. Menetrier, J.M. Tarascon, M. Deschamps, E. Salager, Nat. Commun. 7 (2016) 13284.

[69] X. Li, M. Tang, X. Feng, I. Hung, A. Rose, P.-H. Chien, Z. Gan, Y.-Y. Hu, Chem. Mater. 29 (2017) 8282–8291.

[70] M.A.T. Marple, B.G. Aitken, S. Kim, S. Sen, Chem. Mater. 29 (2017) 8704–8710.

[71] C. Yu, S. Ganapathy, N.J. de Klerk, I. Roslon, E.R. van Eck, A.P. Kentgens, M. Wagemaker, J. Am. Chem. Soc. 138 (2016) 11192–11201.

[72] B.M. Meyer, N. Leifer, S. Sakamoto, S.G. Greenbaum, C.P. Grey, Eletrochem. Solid. St. 8 (2005) A145.